Case Studies in Construction Materials 21 (2024) e03659

Contents lists available at ScienceDirect

Case Studies in Construction Materials

journal homepage: www.elsevier.com/locate/cscm

Effects of Mg-based admixtures on chloride diffusion in alkali-activated fly ash-slag mortars

Jingxiao Zhang [a,b,c,d,*], Yuwei Ma [b,**], Zuhua Zhang [c,**], Xiaocong Yang [b], Xingzhong Nong [a], Hao Wang [d]

[a] Guangzhou Metro Design and Research Institute Co., Ltd., Guangzhou 510010, China
[b] Research Center for Wind Engineering and Engineering Vibration, Guangzhou University, Guangzhou 510006, China
[c] School of Materials Science and Engineering, Tongji University, Shanghai 201804, China
[d] Center for Future Materials, University of Southern Queensland, Toowoomba, QLD 4350, Australia

ARTICLE INFO

Keywords:
Alkali-activated materials
Magnesium oxide (MgO)
Layered double hydroxides (LDH)
Calcined layered double hydroxides (CLDH)
Chloride diffusion

ABSTRACT

This study evaluated the effects of various Mg-based admixtures, including magnesium oxide (MgO), layered double hydroxides (LDH), and calcined layered double hydroxides (CLDH), on the chloride resistance of alkali-activated fly ash-slag (AAFS) mortars. To this end, chloride diffusion tests were conducted on AAFS mortars containing 5 wt% MgO, Mg-Al-CO_3 LDH, and CLDH. The results revealed that all Mg-based admixtures investigated in this study enhanced the chloride resistance of AAFS mortars. The inclusion of MgO led to a finer pore structure and promoted the formation of more Friedel's salt, thereby enhancing the chloride resistance performance. Although the inclusion of Mg-Al-CO_3 LDH and CLDH resulted in more lager pores in the matrix, leading to slightly lower compressive strength, the overall content of Mg-Al LDH and Friedel's salt formed in the system increased, which led to an improved chloride binding capacity and enhanced chloride resistance.

1. Introduction

Commonly employed in various civil infrastructures, reinforced concrete is favoured due to its cost-effectiveness, high compatibility, and wide resource availability [1]. However, the service life of reinforced concrete structures in chloride-containing environments (e.g., seawater and de-icing salts) is typically considerably shorter than their designed service life due to chloride-induced corrosion [1,2]. While chloride ions (Cl^-) typically do not directly harm the concrete matrix, they can easily penetrate into it and reach the surface of the reinforcement steel [2,3]. As the chloride content near the surface of the reinforcement steel rises to the critical chloride content (threshold value), the passive film may partially or entirely break down, consequently triggering the onset of corrosion in the reinforcement steel and decreasing the long-term durability of the reinforced concrete [1,2,4]. To prevent chloride-induced corrosion and extend the service life of reinforced concrete structures, several methods have been implemented, including the use of corrosion inhibitors, the application of functional coatings or paintings, and the implementation of cathodic protection [5]. It is widely accepted that enhancing the pore structure and chloride binding capacity of the concrete matrix are two of the most cost-efficient ways to promote the durability of concretes [6,7]. To achieve these goals, two promising approaches have

* Corresponding author at: Guangzhou Metro Design and Research Institute Co., Ltd., Guangzhou 510010, China.
** Corresponding authors.
E-mail addresses: zhangjingxiao@gmdi.cn (J. Zhang), yuwei_ma@gzhu.edu.cn (Y. Ma), zhangzuhua@tongji.edu.cn (Z. Zhang).

https://doi.org/10.1016/j.cscm.2024.e03659
Received 11 June 2024; Received in revised form 30 July 2024; Accepted 20 August 2024
Available online 21 August 2024

recently been proposed. One involves the utilization of new cementitious materials as substitutes for ordinary Portland cement (OPC) [2], and the other involves modifying the concrete mixtures through the use of admixtures [8].

Alkali-activated materials (AAMs), commonly referred to as geopolymers, are increasingly recognized as promising alternatives to OPC. AAMs are produced through the reaction between aluminosilicate-rich precursors, such as fly ash (FA), metakaolin (MK), and ground granulated blast furnace slag (GGBFS), and alkali activators, such as NaOH, $Na_2O{\cdot}nSiO_2$, and Na_2CO_3 [9]. Known for their low-CO_2 emission profile, these materials are typically categorized into two systems: the low-calcium system and the high-calcium system. In the low-calcium system, such as alkali-activated FA and alkali-activated MK, the primary reaction products are sodium aluminosilicate hydrate (N-A-S-H) gels, characterized by a pseudo-zeolitic network structure [10]. Conversely, in the high-calcium system, represented by alkali-activated GGBFS (AAS), the main reaction products are calcium aluminosilicate hydrate (C-A-S-H) gels that have a tobermorite-like structure [9]. Furthermore, due to the significant amounts of Mg and Al present in GGBFS, it can induce the formation of Mg-Al layered double hydroxides (LDH) and Ca-Al LDH (also known as AFm phase or strätlingite) [9]. Ke et al. [11] reported that these LDHs exhibited effective adsorption of Cl^- from simulated chloride-rich pore solutions. Therefore, these LDHs can be regarded as contributing factors that enhance the chloride binding capacity of AAS. For alkali-activated fly ash-slag (AAFS), previous studies [12,13] indicated that a high GGBFS content ($\geq$ 50 wt%) generally resulted in a more compact microstructure. Consequently, this compact microstructure contributes to higher chloride resistance, surpassing that of OPC. However, the absence of LDH in AAFS leads to a significant lack of chemical chloride binding, which greatly impacts the chloride binding capability at low chloride concentrations [14,15]. As a result, previous studies [13,15,16] reported that the chloride binding capability of AAFS was generally lower than that of OPC when the chloride concentration approximates that of seawater (0.6–0.7 mol/L [17]). Fortunately, compared to the chloride binding capability, the pore structure has a more significant impact on the chloride resistance of AAFS [2]. Therefore, AAFS generally exhibits better chloride resistance than OPC. In the study by Zhang et al. [12], except for the mixtures with a high water/binder mass ratio (w/b), the chloride resistance of all prepared AAFS mixtures was significantly higher than that of OPC.

Layered double hydroxides (LDH), with a general formula of $[M^{2+}_{1-x}M^{3+}_x(OH)_2]^{x+}[A^{n-}_{x/n}]^{x-}{\cdot}mH_2O$, consist of brucite-like layers (where M^{2+} represents divalent metal cations, e.g., Mg^{2+}, and M^{3+} stands for trivalent metal cations, e.g., Al^{3+}), interlayer anions (A^{n-}: n-valent anions, e.g., CO_3^{2-}, OH^-, Cl^-, and NO_3^-), and interlayer water molecules [11]. The molecular structure of LDH is illustrated in Fig. 1. Owing to the partial substitution of M^{2+} by M^{3+}, the brucite-like layers carry a positive charge. Moreover, the interlayer anions, being weakly bonded, can exchange with other anions. Consequently, LDH can both physically adsorb and chemically bind Cl^-. As previously noted, Mg-Al LDH and Ca-Al LDH are commonly observed as secondary products in AAS [9,11]. When GGBFS with a medium or high MgO content (> 5 wt%) is used as the raw material, Mg-Al-OH LDH and Mg-Al-CO_3 LDH are often formed [9,11]. The anion replacement order in Mg-Al LDH is $CO_3^{2-} > OH^- > Cl^-$ [18], indicating that the ion exchange between Cl^- and the intercalated CO_3^{2-} and OH^- is notably challenging [3]. Despite this, Ke et al. [11] proposed that the main binding mechanism of Mg-Al LDH is surface adsorption (90 %) instead of ion exchange (10 %) due to its relatively large surface area. Therefore, the formed Mg-Al-OH LDH and Mg-Al-CO_3 LDH can still adsorb a significant amount of Cl^-, resulting in an enhanced chloride binding capability.

Inspired by the advantages of a high MgO content in GGBFS, the addition of extra Mg is perceived as an effective method to further enhance the chloride resistance of AAMs. Various Mg-based admixtures, including MgO, Mg-Al LDH, and calcined Mg-Al LDH (CLDH), have been utilized to improve the durability of OPC [2]. Choi et al. [20] reported that the incorporation of 5 wt% MgO resulted in a reduction of capillary pores ranging between 30 and 300 nm, thereby affecting both the compressive strength and chloride diffusion. Shui et al. [21] found that while the addition of Mg-Al-NO_3 LDH coarsened the pore structure of OPC concrete, the higher chloride binding capacity of Mg-Al-NO_3 LDH positively influenced the chloride resistance of OPC. Yang et al. [8] compared the impact of Mg-Al-pAB LDH and Mg-Al-NO_2 LDH on the chloride resistance of the OPC mortar, and found that the former had a superior effect. As depicted in Fig. 2, CLDH, calcined from natural hydrotalcite (Mg-Al-CO_3 LDH), can reconstruct the layered double structure in high-alkali environments, such as concrete pore solutions [22,23]. Duan et al. [24] concluded that the addition of 2 wt% CLDH improved the chloride resistance of OPC and sulphoaluminate cement, and attributed this improvement to the chloride binding of the

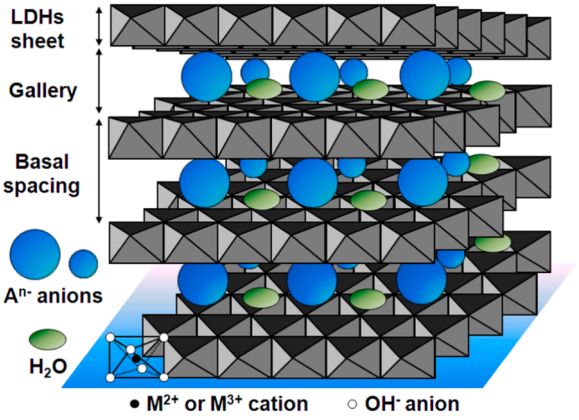

Fig. 1. Structure of layered double hydroxides (LDH).
from [19]

reconstructed LDH.

With regards to the effect of Mg-based admixtures on the chloride resistance of AAMs, relevant studies are limited. Yoon et al. [25] found that while the addition of 5 wt% MgO in AAFS binder (50 wt% GGBFS) increased the total electrical charge in the rapid chloride permeability test (RCPT), it decreased the depth of chloride penetration in the ponding test. Based on the non-steady-state migration (NSSM) test, Liu et al. [26] reported that the incorporation of 4 wt% MgO, Mg-Al-NO_3 LDH, and CLDH could enhance the chloride resistance of AAFS mortars (70 wt% GGBFS). Among these, AAFS with CLDH exhibited the smallest chloride migration coefficient (D_{NSSM}). Ke et al. [27] found that when CLDH particles were incorporated into AAS, they could serve as nucleation seeding points, leading to an enhanced microstructure and a reduction in D_{NSSM}. To minimize test durations and reduce labour requirements, previous studies on the chloride resistance of Mg-modified AAMs predominantly relied on the RCPT and NSSM test. However, these rapid tests primarily concentrated on pore structure and did not sufficiently account for chloride binding [2,28]. In contrast, the chloride diffusion test can consider the influence of chloride binding, thereby providing a more accurate reflection of the actual conditions in submerged zones. Earlier research on Mg-modified OPC [8,21] indicated that the results obtained from chloride diffusion tests were superior to those from rapid tests. This superiority was ascribed to the significant enhancement of Mg-based admixtures on the chloride binding capacity of the matrix. Consequently, it is essential to conduct chloride diffusion tests on Mg-modified AAMs to achieve more realistic and accurate results.

This study aims to explore the effects of various Mg-based admixtures, including MgO, Mg-Al-CO_3 LDH, and CLDH, on the chloride diffusion in AAFS mortars. To gain a deeper understanding of the influence mechanisms of different Mg-based admixtures, the physicochemical properties of Mg-modified AAFS samples were characterized. The contributions of Mg-based admixtures to enhancing the chloride resistance of AAFS mortars were evaluated using bulk diffusion tests. The findings of this research are expected to provide a more scientific foundation for the application of Mg-based admixtures in reinforced AAFS concrete structures exposed to marine environments.

2. Experimental programme

2.1. Materials

In this study, Class F FA (according to ASTM C618) from Zhongshan Electric Power Plant, Guangdong, China, and GGBFS from Shaoguan Steel Factory, Guangdong, China, were utilized as precursors in AAFS samples. PO 42.5 cement, sourced from Yangchun Cement Company Limited, Shandong, China, was employed in OPC reference samples. The chemical compositions of FA, GGBFS, and OPC were determined by X-ray fluorescence (XRF), as depicted in Table 1. A Mastersizer 2000 particle size analyser was used to measure the particle size distribution of FA and GGBFS (Fig. 3). The d_{50} values of FA and GGBFS were 11.67 μm and 14.09 μm, respectively. For the preparation of AAFS and OPC mortars, ISO standard sand, procured from Xiamen ISO Standard Sand Company Limited, Fujian, China, was used as the fine aggregate.

The alkaline activator used in this study was a sodium silicate ($Na_2O{\cdot}nSiO_2$) solution, which was prepared by mixing analytical grade sodium hydroxide (NaOH, > 98 % purity), industrial grade waterglass (Na_2O = 12.19 wt%, SiO_2 = 28.18 wt%, H_2O = 58.92 wt %) and distilled water. Initially, the NaOH powder was dissolved in water to prepare a NaOH solution. Thereafter, the NaOH solution and waterglass were mixed together. The alkali activator was then allowed to cool down and was stored at room temperature (20 °C) for 24 h.

Mg-based admixtures including MgO, Mg-Al-CO_3 LDH, and calcined Mg-Al-CO_3 LDH were used in this study. Analytical grade MgO

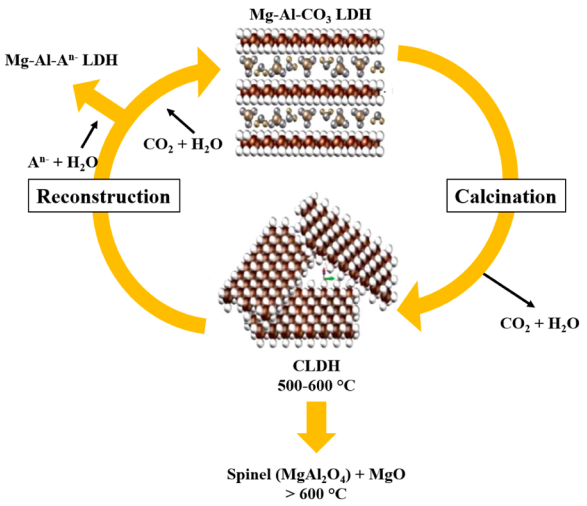

Fig. 2. Calcination and reconstruction of LDH, reproduced from [22,23].

Table 1
Chemical compositions of FA and GGBFS.

	SiO_2	Al_2O_3	CaO	Fe_2O_3	MgO	SO_3	Na_2O	K_2O	LOI[a]
FA	50.59	25.55	9.84	6.92	1.12	1.12	1.45	1.19	2.22
GGBFS	34.36	16.89	38.13	0.36	6.23	2.3	0.24	0.41	1.08
OPC	11.20	5.27	72.83	3.93	2.37	2.30	0.10	1.03	0.97

[a] LOI is Loss on Ignition

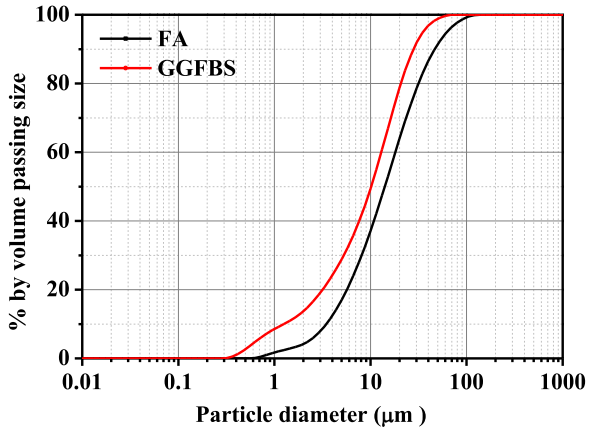

Fig. 3. Particle size distribution of FA and GGBFS.

(> 98 % purity) was provided by Zhiyuan Chemistry Reagent Company Limited, Tianjin, China. Commercial Mg-Al-CO_3 LDH was supplied by Shaoyang Heaven Assistant Chemical Industry Company Limited, Hunan, China. Calcined Mg-Al-CO_3 LDH (abbreviated as CLDH) was prepared by thermally treating Mg-Al-CO_3 LDH at 550 °C for 4 h with a heating rate of 5 °C/min [26,29]. The X-ray diffractometry (XRD) patterns and Fourier transform infrared spectroscopy (FTIR) spectra of Mg-Al-CO_3 LDH and CLDH are presented in Fig. 4. As shown in Fig. 4(a), the main diffraction peaks of Mg-Al LDH were very sharp, especially d(003) at 11.6° and d(006) at 23.4°, indicating a high purity and complete crystal structure [3,24,30,31]. In CLDH, the well-defined diffraction peaks of the original sample were replaced by MgO peaks at 43.4° and 62.9°, consistent with previous studies [24,30,31]. In Fig. 4(b), the broad band at around 3424 cm^{-1} was attributed to physically adsorbed water molecules and hydroxyl groups on brucite-like layers [30,32], which became less intense in CLDH. The strong band observed at 1362 cm^{-1} was due to the $\nu 3$ asymmetric stretching of carbonate anions [30, 31]. This band significantly weakened in CLDH, indicating that most carbonate anions were removed by calcination.

2.2. Sample preparation

AAFS and OPC pastes, along with mortars, were prepared following the mix proportions presented in Table 2. Five sets of pastes were prepared: AAFS pastes without any admixture (P-A), AAFS pastes with 5 wt% MgO (P-M), AAFS pastes with 5 wt% Mg-Al-CO_3

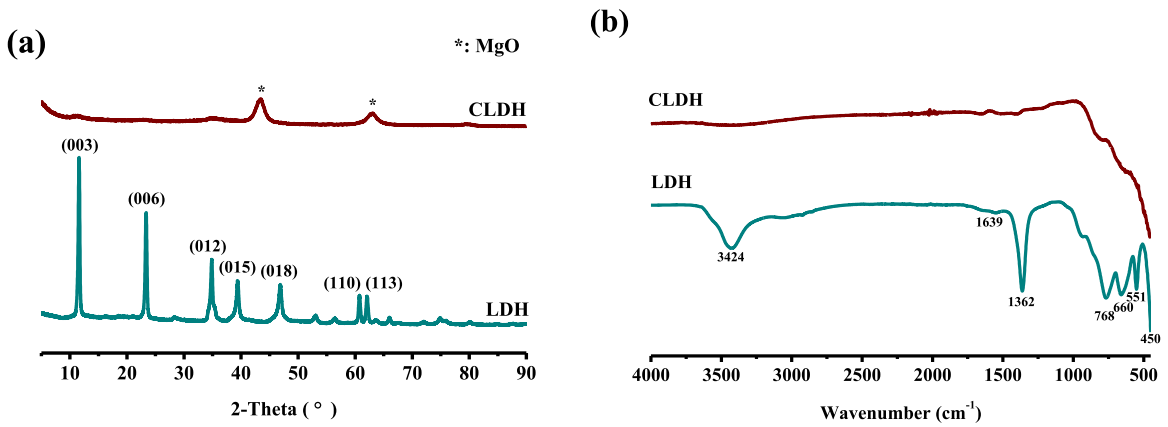

Fig. 4. XRD patterns (a) and FTIR spectra (b) of Mg-Al-CO_3 LDH and CLDH.

LDH (P-L), AAFS pastes with 5 wt% CLDH (P-C), and OPC pastes (P-OPC). The mix proportion of P-A was derived from an AAFS concrete that demonstrated excellent engineering performance in areas such as workability, compressive strength, and chloride resistance [12]. In this mix proportion, the FA/GGBFS mass ratio was maintained at 1:1. The Na_2O and SiO_2 contents provided by the alkali activator were kept at 4 % and 6 % of the total mass of precursors (FA+GGBFS), respectively. The water/binder mass ratio (w/b) was kept at 0.45. Additionally, five sets of mortars (M-A, M-M, M-L, M-C, and M-OPC) were prepared, all featuring the same binder constituents and maintaining a binder/sand mass ratio of 1:2.

AAFS pastes and mortars were prepared utilizing a JJ-5 rotary mixer. To ensure uniform dispersion, the precursors (FA+GGBFS), admixture, and sand (only for mortars) were initially dry mixed for 2 mins at medium speed. Subsequently, the alkali activator was slowly added. The mixture was then mixed for another 2 mins at low speed. After scraping down the blade and bowl, the mixing continued for an additional 2 mins at medium speed. Following this, the paste was poured into plastic bottles (Ø 36 mm × 68 mm), while the mortar was cast into cubic moulds (40 mm × 40 mm × 40 mm and 70 mm × 70 mm × 70 mm). These bottles and cubic moulds were vibrated for 2 mins to eliminate air bubbles and subsequently sealed to prevent moisture loss. After a curing period of 24 h at room temperature (20 °C), the paste and mortar samples were demolded and transferred to a curing chamber (relative humidity of 95 % and temperature of 20 ± 2°C) until the testing day. OPC reference samples were also prepared following the same steps.

2.3. Testing methods

2.3.1. Compressive strength

Following the guidelines of NEN-EN-196–1, the compressive strength of AAFS and OPC mortar cubes (40 mm × 40 mm × 40 mm) was measured at 3, 7, 28, and 63 days. The compression load was applied by an Instron-5984 universal testing machine (Instron, UK) at a rate of 2.4 kN/s. For each mix proportion and at each testing age, the average result was calculated from at least three replicates.

2.3.2. Mercury intrusion porosimetry (MIP)

Mercury intrusion porosimetry (MIP) was utilized to determine the total porosity and pore size distribution of AAFS and OPC mortars [12,33]. After a curing period of 28 days, the mortar specimens were crushed. Fragments from the center of these specimens were selected and broken down into smaller pieces (about 3 mm^3). To halt further alkali-activation, these pieces were immersed in isopropanol for 24 h, and subsequently dried in an oven at 60 °C until reaching a constant mass [33]. MIP measurements were conducted using an Autopore IV 9500 mercury intrusion porosimeter (Micromeritics, USA), applying a pressure range from 0.51 psia to 61,000.00 psia. The measurements were taken with a contact angle of 130° and a surface tension of 0.485 N/m.

2.3.3. Nitrogen adsorption test

To complement the results of MIP, nanoscale pores were examined by conducting a nitrogen adsorption test using an ASAP 2460 surface area and porosimetry analyser (Micromeritics, USA). In accordance with the method detailed above for preparing MIP mortar samples, AAFS and OPC pastes after a curing period of 28 days were crushed into small pieces of 1–2 mm^3, and the reaction was subsequently halted through a solvent exchange. Prior to conducting the nitrogen adsorption test, these paste samples were degassed at 60 °C. The Barrett-Joyner-Halenda (BJH) model was utilized to calculate the pore size distribution [34].

2.3.4. X-ray diffractometry (XRD)

To identify potential chemical binding products, powder samples from AAFS and OPC pastes, after immersion in a simulated chloride-rich pore solution, were analysed by X-ray diffractometry (XRD). The simulated chloride-rich pore solution was prepared in accordance with previous studies [11,27], as detailed in Table 3. The chloride concentration was maintained at 0.75 mol/L, slightly higher than that found in seawater (0.6–0.7 mol/L) [15,17].

After 28 days of curing, AAFS and OPC pastes were broken into pieces. The fragments from the center were further crushed in sealed plastic bags using a hammer [27], then sieved to obtain particles within a size range of 0.25–0.90 mm. 2 g of sieved paste particles were promptly added to 12 mL of simulated chloride-rich pore solution in 15 mL centrifuge tubes. These tubes were sealed to

Table 2
Mix proportions of AAFS and OPC pastes (P) and mortars (M).

Sample ID	Binder			Activator			Admixture			Sand (wt %)
	FA (wt %)	GGBFS (wt %)	Cement (wt %)	Na_2O (wt %)	SiO_2 (wt %)	w/b	MgO (wt %)	Mg-Al-CO_3 LDH (wt%)	CLDH (wt %)	
P-A	50	50		4 %	6 %	0.45				
P-M	50	50		4 %	6 %	0.45	5 %			
P-L	50	50		4 %	6 %	0.45		5 %		
P-C	50	50		4 %	6 %	0.45			5 %	
P-OPC			100			0.45				
M-A	50	50		4 %	6 %	0.45				200
M-M	50	50		4 %	6 %	0.45	5 %			200
M-L	50	50		4 %	6 %	0.45		5 %		200
M-C	50	50		4 %	6 %	0.45			5 %	200
M-OPC			100			0.45				200

Table 3
Stoichiometric compositions of simulated chloride-rich pore solution.

NaCl (mol/L)	NaOH (mol/L)	Total Na^+ (mol/L)	$[Cl^-]/[OH^-]$
0.75	0.25	1.00	3.0

minimise water evaporation and prevent sample carbonation. The immersion period lasted 60 days, during which the centrifuge tubes were intermittently shaken for 2 min every 3 days to ensure reaction equilibrium [15]. The storage temperature was maintained at 20 ± 2 °C [15,35]. After immersion, the particles were separated from the simulated chloride-rich pore solution, washed with distilled water, ground into fine powders, and sieved using a 0.045 mm mesh. Finally, the powders were dried in an oven at 60 °C for 2 h. For XRD analysis, a PW 3040/60 X'Pert Pro powder diffractometer (PANalytical, Netherland) equipped with Cu-Kα radiation (λ = 1.5418 Å) was used. The powder samples underwent step-scanning in the range of 10–35° 2θ. The step size was set at 0.02°, and the count time was 2 s/step. As reference samples, powders from non-immersed samples were also tested.

2.3.5. Chloride diffusion test

Bulk diffusion tests were conducted on AAFS and OPC mortar cubes (70 mm × 70 mm × 70 mm) in accordance with ASTM C1556. After a curing period of 28 days, the surfaces of each mortar cube were sealed with paraffin wax, leaving only one surface unsealed to facilitate one-dimensional diffusion [36]. Subsequently, these sealed mortar cubes were immersed in a 165 g/L NaCl solution for a period of 35 days. A DRB-H1 concrete grinding machine was used to obtain powder samples. After the removal of paraffin wax, 10 layers, each 2 mm thick, were ground from the exposed surface of each mortar cube. The powder samples were then sieved using a 0.6 mm sieve, dried in an oven at 55 °C for 2 h, and subsequently cooled to 20 °C in a desiccator [12,37]. Afterwards, the powder samples were sealed and stored until the testing day. As per JTJ270–98, the free (water-soluble) chloride content of each powder sample was determined using $AgNO_3$ titration, thereby obtaining the chloride profile [12,37]. The choice of free chloride content over total chloride content is because bound chloride ions are completely removed from the pore solution and do not contribute to the induction or enhancement of reinforcement steel corrosion [2].

Upon completing the bulk diffusion test and titration, the apparent chloride diffusion coefficient (D) was determined. This was achieved by fitting the measured chloride profile to Fick's second law, as expressed in Eq. (1), through a non-linear regression analysis using MATLAB.

$$c(x,t) = c_0 + (c_s - c_0)[1 - erf\left(\frac{x}{2\sqrt{D \bullet t}}\right)] \quad (1)$$

where:

$C(x,t)$ is chloride content (mass %) at depth x (m) and time t (s); C_0 is initial chloride content (mass %); C_s is exposure surface chloride content (mass %); D is apparent chloride diffusion coefficient (m^2/s); and erf is error function.

3. Results and discussion

3.1. Compressive strength

Fig. 5 presents the compressive strength of AAFS and OPC mortars at 3, 7, 28 and 63 days. As expected, the compressive strength of all mortars increased with curing age. This can be reasonably attributed to the continuous reaction and the enhancement of the pore structure. While performance at 3 days was relatively weak, after 7 days, the compressive strength of all AAFS mortars (except for M-L) exceeded that of the OPC sample (M-OPC). At 28 days, the compressive strength of the unmodified AAFS mortar (M-A) was 60.43 MPa,

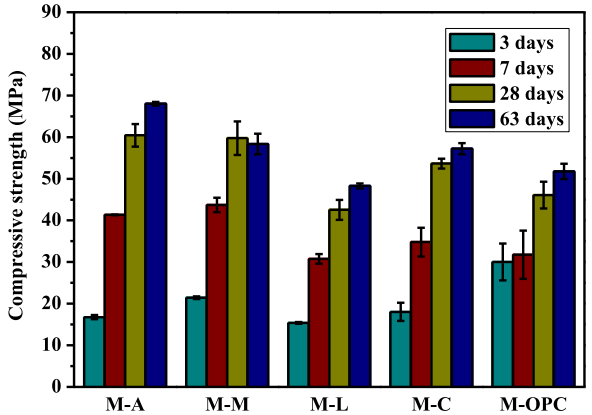

Fig. 5. Compressive strength of AAFS and OPC mortars at 3, 7, 28 and 63 days.

which was approximately 131 % of that of M-OPC (46.08 MPa).

As shown in Fig. 5, the addition of 5 wt% MgO significantly improved the early-age compressive strength of the AAFS mortar (M-M), with an increase of 28 % at 3 days and 6 % at 7 days, respectively. This trend is consistent with previous studies [26, 38–40]. It was reported that MgO promoted the reaction and produced more reaction products to fill the capillary pores [38,39]. However, the use of MgO was not effective in enhancing the compressive strength at later stages. At 28 days, the compressive strength of M-M was surpassed by that of M-A. Subsequently, the compressive strength of M-M even regressed. This may be attributed to the fact that MgO can form expansive phases, leading to cracking and volume instability in the matrix [40].

The direct application of Mg-Al-CO_3 LDH in the AAFS mortar led to reduced mechanical properties, as shown in Fig. 5. At 28 days, the compressive strength of M-L (42.54 MPa) was about 70 % of that of M-A (60.43 MPa), and even lower than that of M-OPC (46.08 MPa). Similar results were also reported in other studies [8,26]. Liu et al. [26] found that the use of 2–4 wt% Mg-Al-NO_3 LDH resulted in a slight decrease in the compressive strength of the AAFS mortar (with a FA/GGBFS mass ratio of 3:7). Moreover, Yang et al. [8] reported that the addition of 5–10 wt% Mg-Al-pAB LDH and Mg-Al-NO_2 LDH significantly reduced both the compressive strength and flexural strength of the OPC mortar. The possible reason might be the production of more air voids. This hypothesis will be further justified through the characterization of the pore structure in the later section. The introduction of CLDH into the AAFS mortar was beneficial to the compressive strength in the first three days (Fig. 5). However, after 7 days, the compressive strength of M-C was surpassed by that of M-A. Compared with Mg-Al-CO_3 LDH, the negative impact of CLDH on compressive strength was relatively less pronounced. Finally, M-C (57.23 MPa) exhibited a compressive strength similar to that of M-M (58.35 MPa), both of which were about 84–86 % of the compressive strength of M-A (68.03 MPa). Ke et al. [29] claimed that Mg-Al-OH LDH, formed via reconstruction, could act as a nucleation seed to promote gel precipitation. This might lead to a faster reaction in the early stages and fewer air voids in the later stages.

3.2. Pore structure

Like other cementitious materials, the AAFS binder is not completely impenetrable and contains several types of pores that influence both compressive strength and ionic transport. According to traditional classification [41], these pores can be divided into three categories: gel pores (<10 nm), capillary pores (10–10,000 nm), and air voids (>10,000 nm). It is generally regarded that gel pores, being the smallest, are found in reaction products and primarily affect shrinkage and creep [33]. Entrapped/entrained air voids, while being the largest, can be harmful to mechanical properties. However, due to their low volume fraction and lack of interconnectivity, they generally do not influence transport properties [42]. Among all the pore types, capillary pores (including large gel pores) are of the greatest significance in terms of strength and ionic transport, due to their high volume fraction, relatively large size and interconnectivity [33,42].

The pore size distribution of AAFS and OPC mortars, derived from MIP, is depicted in Fig. 6. As shown in Fig. 6(A), the total porosity of the OPC mortar (M-OPC, 17.138 %) was significantly higher than that of almost all AAFS mortars, which ranged from 12.313 % to 13.387 %. The only exception was the LDH-modified AAFS mortar (M-L), which had a total porosity of 18.519 %. Fig. 6(B) reveals that the capillary pores in M-OPC primarily ranged between 10 and 200 nm. In contrast, those in AAFS mortars predominantly spanned a significantly larger range of 200–10,000 nm. This observation aligns with previous studies [26,43]. Interestingly, despite having a larger pore size, AAFS mortars exhibited a smaller total volume of capillary pores (8.306 %-10.586 %) compared to M-OPC (14.672 %). This finding corroborates those observed in AAFS mortars containing 70 wt% GGBFS [26].

The volume of capillary pores in the MgO-modified AAFS samples (M-M) exhibited a minor decrease. This observation is consistent with findings for MgO-modified OPC [20] and AAS [38–40]. This likely indicates that gels formed rapidly, filling the capillary pores. This is further supported by the enhanced early-age compressive strength evident in Fig. 5. The mechanism behind the acceleration of alkali-activation by MgO addition may be linked to its dissolution, leading to a rapid heat release and an elevated pH [38,44]. The

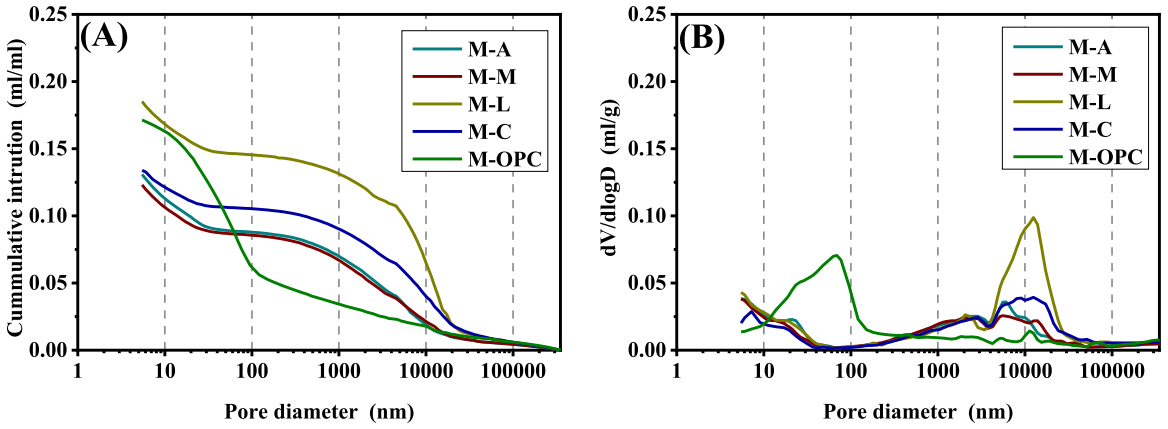

Fig. 6. Pore size distribution of AAFS and OPC mortars, derived from MIP.

inclusion of Mg-Al-CO_3 LDH and CLDH led to an increase in total pore porosity, suggesting a coarser pore structure. This was primarily due to the presence of a greater number of air voids (>10,000 nm). Reduced workability and uneven distribution of LDH and CLDH may have contributed to this outcome [8]. However, since these air voids are not interconnected, their impact on chloride diffusion remains limited [42,45]. Compared to M-L, M-C exhibited a smaller volume of air voids, which is consistent with the lower compressive strength depicted in Fig. 5. As previously mentioned, this may be attributable to the reconstructed Mg-Al LDH from CLDH serving as a nucleation seed that promoted gel precipitation [29], while the directly added Mg-Al-CO_3 LDH was largely inert in the reaction.

Fig. 7 illustrates the nitrogen adsorption-desorption isotherms and the pore size distribution of AAFS and OPC pastes. In Fig. 7(A), the isotherms for all mixes displayed a hysteresis loop. This phenomenon can be attributed to the capillary action of N_2 in pores ranging from 2 to 50 nm [46,47]. These hysteresis loops did not level off at relative pressures nearing the saturation vapor pressure, indicating the presence of slit-like pores in materials consisting of plate-like particles [46,47]. In Fig. 7(B), the sizes of most pores were below 10 nm, categorizing them as gel pores. The difference in critical pore size between mixes was marginal. Compared to other mixes, P-C contained fewer gel pores. This difference might stem from either a reduced number of reaction products or a more compact product structure [46,48]. Given the MIP results from Fig. 6, the latter explanation seemed more plausible.

3.3. Phase composition

The XRD patterns of AAFS and OPC pastes, both before and after 60 days of immersion in the simulated chloride-rich pore solution, are presented in Fig. 8. All mixes exhibited low intensity peaks around 29.3° 2θ, indicating the presence of poorly crystalline C-S-H (PDF# 00–034–0002) and C-(A)-S-H (PDF# 00–033–0306) as the primary reaction products of OPC and AAFS, respectively [16,49]. These primary reaction products, due to Van der Waals and/or electrostatic forces, can physically adsorb chloride ions [2,16]. However, their chloride binding capacity is much lower compared to Mg-Al LDH and Ca-Al LDH [3,11]. Similar to previous research results [15], Friedel's salt ($Ca_2Al(OH)_6Cl{\cdot}2\ H_2O$, PDF# 00–042–0558), known as Ca-Al LDH, was detected after reaching adsorption equilibrium in P-OPC (Fig. 8(b)). This indicates that chemical binding is another mechanism of interaction between Portland cement and chloride ions [2,16]. Friedel's salt was also observed in the unmodified AAFS (P-A) after reaching adsorption equilibrium. This is believed to be a transformation from the poorly crystalline AFm phase [27]. The poorly crystalline AFm phase is not always identifiable by XRD [9,11], as shown in Fig. 8(a). However, the peak intensity observed in AAFS was lower than that in OPC. This observation aligns with earlier studies [13,15,16], which reported that the bound chloride content in AAFS containing 50 wt% GGBFS was typically lower than that of OPC when exposed to the concentration of seawater (0.6–0.7 mol/L [17]).

The introduction of various Mg-based admixtures resulted in the emergence of Mg-Al LDH ($Mg_6Al_2(OH)_{16}CO_3{\cdot}4\ H_2O$, PDF# 00–014–0191) and/or an increased presence of Friedel's salt. Due to their similar structures, Mg-Al LDH and Friedel's salt are frequently mistaken for one another. However, their XRD patterns reveal subtle distinctions [15]. Unlike what was detected in AAS [38–40], the formation of Mg-Al LDH was not observed in P-M. The possible reason is the use of $Na_2O{\cdot}nSiO_2$ solution as an activator. On one hand, the lower initial pH of the $Na_2O{\cdot}nSiO_2$ solution may be unfavourable to the formation of Mg-Al LDH [50,51]. On the other hand, the higher Si content in the $Na_2O{\cdot}nSiO_2$ solution may enhance the incorporation of Al into the primary reaction products, thereby reducing the availability of Al for forming Mg-Al LDH [50]. Additionally, the increased Si content dissolved from FA may have similar effects. However, as illustrated in Fig. 8(b), introducing 5 wt% MgO notably heightened the intensity of the peak corresponding to Friedel's salt, surpassing even that in P-OPC. For this phenomenon, Park et al. [44] posited that while a minor increase in MgO content might not be sufficient to produce Mg-Al LDH, it expedited the reaction. This acceleration led to a greater availability of Al, forming more poorly crystalline AFm phase. More poorly crystalline AFm phase, in turn, resulted in more Friedel's salt following

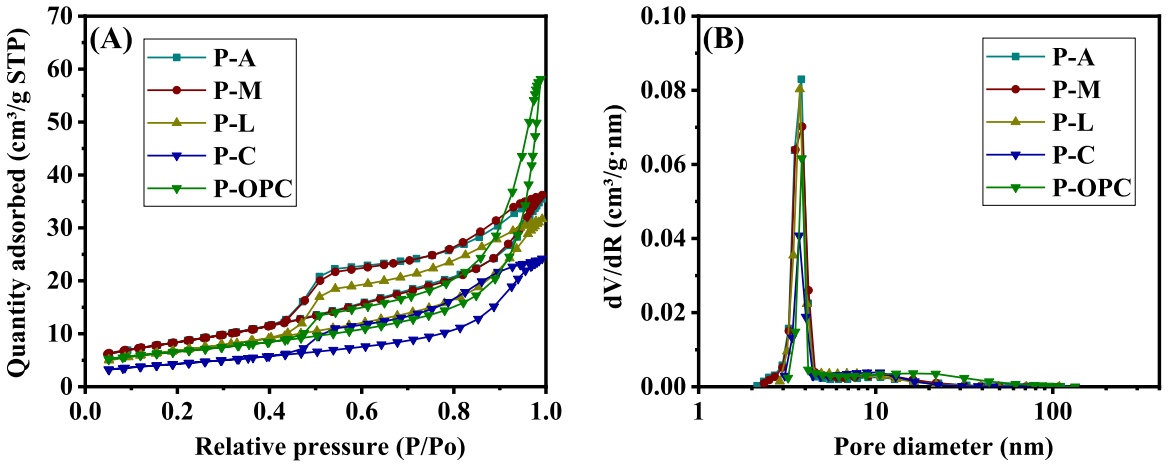

Fig. 7. Nitrogen adsorption-desorption isotherms (A) and desorption pore size distribution (B) of AAFS and OPC pastes, derived from nitrogen adsorption test.

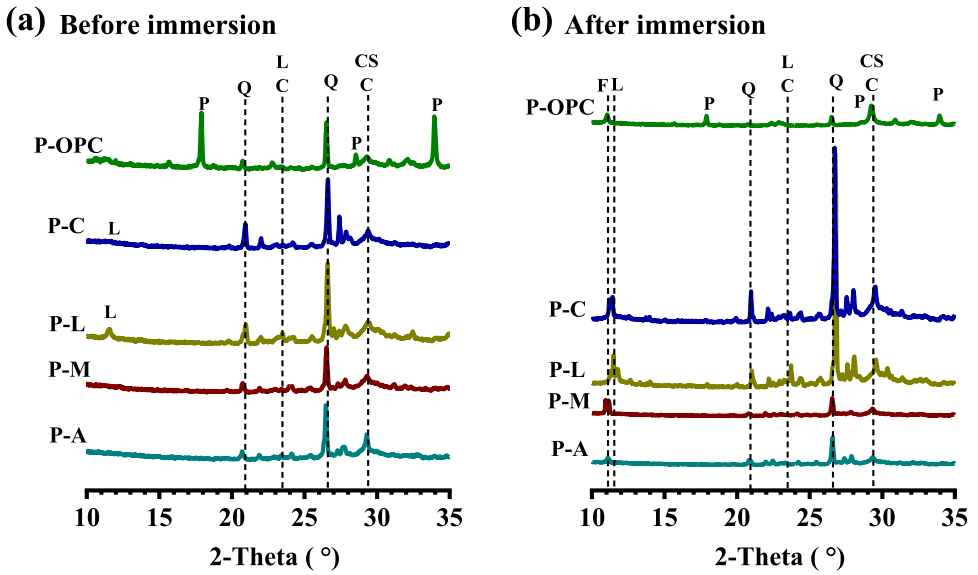

Fig. 8. XRD patterns of AAFS and OPC pastes before (a) and after (b) 60 days of immersion in simulated chloride-rich pore solution. L: Mg-Al-CO_3 LDH ($Mg_6Al_2(OH)_{16}CO_3{\cdot}4\ H_2O$, PDF# 00–014–0191); P: portlandite ($Ca(OH)_2$, PDF# 00–044–1481); Q: quartz (SiO_2, PDF# 01–079–1910); C: calcite ($CaCO_3$, PDF# 01–071–3699); CS: C-S-H (PDF# 00–034–0002)/C-(A)-S-H (PDF# 00–033–0306); F: Friedel's salt ($Ca_2Al(OH)_6Cl{\cdot}2\ H_2O$, PDF# 00–042–0558).

ion-exchange.

In both P-L and P-C, Mg-Al LDH was identified alongside Friedel's salt, as shown in Fig. 8(b). These observations are consistent with prior studies [26,27,29]. When compared to P-A and P-M, the peak intensity for Friedel's salt in P-L and P-C was notably diminished. This matches the findings from AAS with a 5 wt% CLDH addition [27]. However, the introduction and subsequent reconstruction of Mg-Al LDH resulted in the total LDH content (Mg-Al LDH + Ca-Al LDH) in P-L and P-C exceeding that of the unmodified AAFS sample (P-A). Ke et al. [11] found that at high chloride concentrations, the chloride binding capacity of synthetic Mg-Al LDH surpassed that of Ca-Al LDH. This indicates that the increase in Mg-Al LDH improves chloride binding capacity more effectively than the same amount of Ca-Al LDH (i.e., Friedel's salt). Consequently, the enhanced content of LDHs in P-L and P-C improved the chloride binding capacity. When contrasting P-C with P-L, the peak intensity for Mg-Al LDH in P-C was lower, suggesting a limited availability of Mg-Al LDH for chloride binding. A plausible reason could be that the reconstructed Mg-Al LDH acted as a nucleation seed, promoting gel precipitation initially [29], potentially disrupting the further reformation of Mg-Al LDH. It is important to highlight that if a majority of the reconstructed Mg-Al LDH was encapsulated by gels, the chloride ions, mainly present in capillary pores, might not be effectively adsorbed.

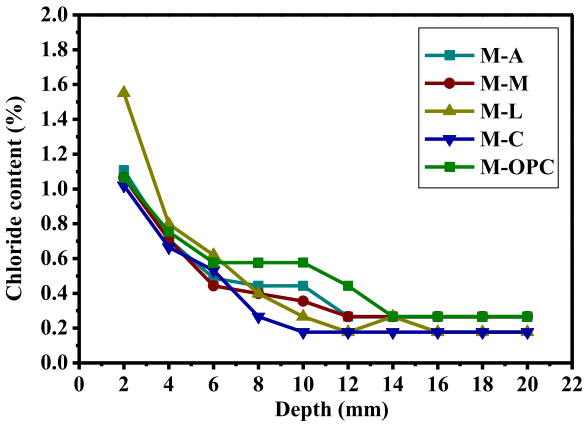

Fig. 9. Comparison of chloride profiles of AAFS and OPC mortars after 35 days of immersion in 165 g/L NaCl solution.

3.4. Chloride diffusivity

3.4.1. Chloride profiles

Fig. 9 presents a comparison of the chloride profiles between AAFS and OPC mortars. Near the exposure surface, there was a sharp decline in the chloride content as the diffusion depth increased. This decrease gradually slowed until it reached a relatively constant value, representing the initial chloride content (C_0). Notably, while not immediately apparent near the exposed surface, the chloride content in M-OPC surpassed that in AAFS mortars. At a depth of 10 mm, M-OPC clearly exhibited the highest chloride content, followed in sequence by M-A, M-M, M-L, and M-C. This observation is consistent with the conclusions of previous research [52,53]. A probable explanation is the presence of more continuous capillary pores in OPC, primarily ranging between 10 and 200 nm, as evidenced by the MIP results depicted in Fig. 6.

The addition of 5 wt% MgO and CLDH led to a slight decrease in the chloride content near the exposed surface. As the diffusion depth exceeded 8 mm, the enhancement effect of CLDH became more pronounced. M-L displayed a higher chloride content within the first 6 mm depth, likely due to the increased presence of air voids, as suggested by the MIP tests (Fig. 6). However, the chloride content in the deeper layers diminished sharply, resulting in a reduced final stability value. This behaviour is consistent with that of the OPC mortar containing 5 wt% Mg-Al-pAB LDH [8]. A possible explanation is that these air voids are not interconnected, thus preventing the creation of continuous pathways for chloride migration [42]. In comparison to other mortar samples, the initial chloride content (C_0) of M-L and M-C was lower. This could be attributed to the addition or reconstruction of Mg-Al LDH, which can chemically bind a significant amount of chloride ions, as indicated by the XRD patterns (Fig. 8). It is important to highlight that when using the total (acid-soluble) chloride content in the bulk diffusion test, as opposed to the free (water-soluble) chloride content, a heightened chloride binding capacity might yield less ideal measurement outcomes [8]. However, the free chloride ions in the pore solution that can cause steel reinforcement corrosion are fewer [2].

3.4.2. Chloride diffusion coefficients (D)

By fitting Fick's second law, as expressed in Eq. (1), to the chloride profiles, the exposure surface chloride content (C_s) and the apparent chloride diffusion coefficients (D) can be determined. Fig. 10 illustrates the fitting curves of AAFS and OPC mortars. As observed, all mixes had a determined coefficient (R^2) exceeding 0.93. Compared to M-OPC, most AAFS mixes exhibited a higher C_s, consistent with prior findings [52]. Yet, the C_s of M-L (2.16 %) was significantly higher than that of other AAFS mixes (around 1.43 %), corresponding to the increased chloride content near the exposure surface. However, due to the pronounced decrease in chloride content with increasing depth, M-L had a notably low C_0.

The apparent chloride diffusion coefficients (D) of AAFS and OPC mortars are presented in Fig. 11. The D of M-A (4.17×10^{-12} m^2/s), without any Mg-admixtures addition, was approximately 41 % of that of M-OPC (10.18×10^{-12} m^2/s). This indicates the superior chloride resistance of AAFS mixes. This observation is consistent with the results of previous chloride diffusion tests, including bulk diffusion tests [14,52], natural chloride diffusion tests [12], and ponding tests [16]. Furthermore, the incorporation of all Mg-based admixtures resulted in a decrease in the D value of the AAFS mortar, a result consistent with findings from the NSSM test [26]. This indicates that all Mg-based admixtures used in this study effectively enhanced the chloride resistance of the AAFS mortar, suggesting that the selected dosage (5 wt%) was appropriate.

As shown in Fig. 11, the addition of 5 wt% MgO significantly enhanced the chloride resistance of the AAFS mortar. The D of M-M (3.31×10^{-12} m^2/s) was approximately 21 % lower than that of M-A (4.17×10^{-12} m^2/s). Consistent results were seen in both the ponding test [25] and the NSSM test [26]. In the ponding test, Yoon et al. [25] determined that introducing 5 wt% MgO reduced the chloride penetration depth of the AAFS binder from 3.9 mm to 3.5 mm. Similarly, Liu et al. [26] found that incorporating 2 wt% and 4 wt% MgO reduced the D_{NSSM} of the AAFS mortar by 14 % and 16 %, respectively. Given these results, it is evident that increasing MgO content can enhance the chloride resistance of AAFS. However, the addition of MgO should not be excessive. Yoon et al. [25]

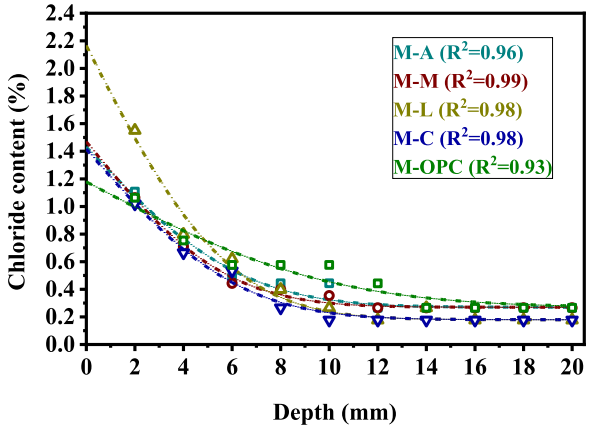

Fig. 10. Fitting curves of AAFS and OPC mortars after 35 days of immersion in 165 g/L NaCl solution.

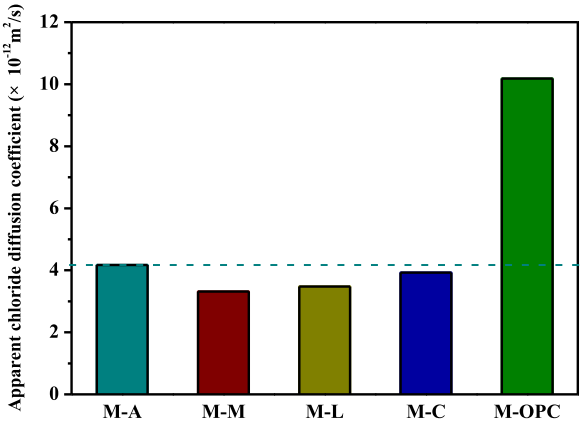

Fig. 11. Apparent chloride diffusion coefficients (D) of AAFS and OPC mortars after 35 days of immersion in 165 g/L NaCl solution.

suggested that adding 10 wt% MgO increased the chloride penetration depth. One possible reason for this is the microcracks caused by the expansion of the hydration products of MgO [54].

The *D* of M-L (3.48×10^{-12} m^2/s) was roughly 83 % of that of M-A (4.17×10^{-12} m^2/s). This indicates that the addition of 5 wt% Mg-Al-CO_3 LDH enhanced the chloride resistance of the AAFS mortar, even though it negatively affected the development of compressive strength during this period (Fig. 5). This finding aligns with previous studies on other variants of Mg-Al LDH [8,21,26]. In the NSSM test, Liu et al. [26] found that the incorporation of 4 wt% Mg-Al-NO_3 LDH reduced the D_{NSSM} of the AAFS mortar by 17 %. This outcome aligns with results from the bulk diffusion test in OPC concrete [21]. Furthermore, Yang et al. [8] examined the effect of 5 wt% Mg-Al-pAB LDH and Mg-Al-NO_2 LDH on chloride ingress in the OPC mortar using the NSSM test, and found that the D_{NSSM} decreased by 12 % and 7 %, respectively.

The inclusion of 5 wt% CLDH also hindered chloride diffusion in the AAFS mortar, a result that is consistent with findings from the NSSM test [26]. Similar observations were made in other materials, including AAS, OPC, and sulphoaluminate cement [24,27,55]. However, the *D* of M-C (3.93×10^{-12} m^2/s) was larger than that of M-M (3.31×10^{-12} m^2/s) and M-L (3.48×10^{-12} m^2/s), indicating that the enhancement effect of CLDH was relatively inferior. Interestingly, this outcome contradicts the smaller D_{NSSM} measured by the NSSM test [26]. A plausible reason for this discrepancy might be that, unlike the NSSM test, the bulk diffusion test can account for chloride binding [28]. Furthermore, the ranking of chloride resistance (M-M > M-L > M-C > M-A > M-OPC) was different from that of compressive strength (M-A > M-M > M-C > M-OPC > M-L). This discrepancy needs to be explained from the perspective of microstructure in subsequent sections.

3.5. *Influence mechanisms of different Mg-based admixtures*

From the experimental results, all the Mg-based admixtures used in this study showed a beneficial effect on the chloride resistance of AAFS mortars (Fig. 11), even though some seemed to have an adverse impact on the compressive strength development (Fig. 5). With the integration of microstructural considerations, the influence mechanisms of these various Mg-based admixtures on chloride diffusion can be discussed.

3.5.1. *Influence mechanisms of MgO*

In comparison to Mg-Al-CO_3 LDH and CLDH, the addition of MgO more effectively enhanced the chloride resistance of AAFS mortars (Fig. 11). This improvement can be attributed to the enhanced pore structure and increased chloride binding capacity. On one hand, the added MgO accelerated the alkali-activation, leading to the formation of more reaction products that subsequently filled the capillary pores [38,44]. The decline in the volume of these capillary pores can be evidenced by Fig. 6. Importantly, among various factors, the volume fraction and connectivity of capillary pores are pivotal [42,56]. Hence, the ability of MgO to fill these pores, thereby reducing their volume fraction and connectivity, can highlight its effectiveness in bolstering chloride resistance. On the other hand, even though the addition of 5 wt% MgO was insufficient to form Mg-Al LDH in AAFS due to the use of the $Na_2O{\cdot}nSiO_2$ solution and the incorporation of FA, it expedited the reaction. The faster reaction rate led to an increased availability of Al [44]. Consequently, a higher amount of AFm phase was formed, which then resulted in a greater quantity of Friedel's salt after ion-exchange, as shown in Fig. 8(b). This process enhanced the chloride binding capacity, further bolstering the chloride resistance of M-M.

3.5.2. *Influence mechanisms of Mg-Al-CO_3 LDH and CLDH*

Although the addition of 5 wt% Mg-Al-CO_3 LDH and CLDH did not bolster the compressive strength of the AAFS mortar (Fig. 5), it proved beneficial for enhancing chloride resistance (Fig. 11). The incorporation of Mg-Al-CO_3 LDH and CLDH resulted in numerous air voids (Fig. 6), leading to a reduction in compressive strength. However, these air voids, unlike capillary pores, are characterized by a significantly smaller volume fraction and a lack of interconnectivity, thereby minimally impacting chloride diffusion [42,45]. As per the XRD analysis (Fig. 8), the introduction and reconstruction of Mg-Al LDH increased the overall content of LDHs (Mg-Al LDH + Ca-Al

LDH) in P-L and P-C, improving the chloride binding capacity. This enhancement is corroborated by the reduced C_0 of M-L and M-C in the chloride profiles (Fig. 9). Given that the increased chloride binding capacity's beneficial effect surpassed the adverse consequence of the rise in air voids, the chloride resistance of M-L and M-C outperformed that of M-A. These findings echo similar research outcomes on OPC [21].

When comparing M-L to M-C, the former displayed a reduced D (Fig. 11). This might seem counterintuitive given M-L's increased air voids (Fig. 6) and diminished compressive strength (Fig. 5). However, the key lies in M-L's enhanced chloride binding capacity. The XRD analysis (Fig. 8) reveals that the peak corresponding to Mg-Al LDH in P-L was more defined than that in P-C, suggesting a more abundant presence of Mg-Al LDH in P-L available for chloride adsorption. The limited presence of Mg-Al LDH in P-C could be attributed to the initially reconstructed Mg-Al LDH acting as a nucleation seed and subsequently being enveloped by gels [29]. This phenomenon might deter further reconstruction of Mg-Al LDH. Moreover, the reconstructed Mg-Al LDH in M-C might be encapsulated by gels, restricting its ability to absorb chloride ions primarily present in capillary pores [2].

4. Conclusions

This study investigated the effects of different Mg-based admixtures (MgO, Mg-Al-CO_3 LDH, and CLDH) on chloride diffusion in AAFS mortars. A strong correlation was identified between chloride resistance and multiple physicochemical characteristics. The main conclusions can be summarized as follows:

1) Introducing 5 wt% MgO, Mg-Al-CO_3 LDH, and CLDH did not improve the compressive strength of AAFS mortars. Although MgO and CLDH contributed to an increased early compressive strength, they had a detrimental effect on the compressive strength development at later stages. Mg-Al-CO_3 LDH significantly decreased the compressive strength of AAFS mortars throughout all ages, falling short even when compared to the OPC reference sample.
2) Relative to OPC, AAFS displayed a decreased total pore volume and a reduced number of capillary pores. The incorporation of 5 wt % MgO into AAFS facilitated the formation of more reaction products to fill capillary pores. Meanwhile, the introduction of 5 wt% Mg-Al-CO_3 LDH and CLDH led to an increase in air voids in AAFS, predominantly influencing compressive strength rather than chloride diffusion.
3) Both OPC and AAFS exhibited the presence of Friedel's salt (Ca-Al LDH). The addition of 5 wt% MgO in AAFS resulted in an increase in Friedel's salt rather than Mg-Al LDH. The incorporation of 5 wt% Mg-Al-CO_3 LDH and CLDH increased the overall content of Mg-Al LDH and Ca-Al LDH in AAFS, especially the former.
4) Chloride diffusion tests indicated that AAFS mortars possessed a distinct advantage in chloride resistance relative to the OPC reference sample. The addition of all Mg-based admixtures at 5 wt% bolstered the chloride resistance of AAFS mortars. Among them, MgO stood out, demonstrating the most pronounced improvement, surpassing both Mg-Al-CO_3 LDH and CLDH in effectiveness.
5) Incorporating MgO resulted in a more refined pore structure and an elevated chloride binding capacity, both factors significantly enhancing the chloride resistance of AAFS mortars. While the introduction of Mg-Al-CO_3 LDH and CLDH led to more air voids, their amplified chloride binding capacity had a more pronounced beneficial impact on chloride resistance. This effect was notably more evident in M-L compared to M-C.

CRediT authorship contribution statement

Jingxiao Zhang: Writing – original draft, Visualization, Investigation, Data curation. **Zuhua Zhang:** Conceptualization. **Yuwei Ma:** Writing – review & editing, Methodology, Conceptualization. **Xingzhong Nong:** Project administration. **Xiaocong Yang:** Investigation. **Hao Wang:** Supervision.

Declaration of Competing Interest

The authors declare that they have no known competing financial interests or personal relationships that could have appeared to influence the work reported in this paper.

Data Availability

Data will be made available on request.

Acknowledgements

The authors sincerely appreciate the financially supported from the National Natural Science Foundation of China (No. 52078149, 52378227, U2001225), the Bureau of Education of Guangzhou (No. SL2022A03J00938, 202255464), the 111 Project (No. D21021), and the Science and Technology Innovation Plan of the Department of Housing and Urban-Rural Development of Guangdong Province (No. 2022-K2–254693).

References

[1] X. Ming, Q. Liu, M. Wang, Y. Cai, B. Chen, Z. Li, Improved chloride binding capacity and corrosion protection of cement-based materials by incorporating alumina nano particles, Cem. Concr. Compos. 136 (2023) 104898.
[2] J. Zhang, Y. Ma, J. Hu, H. Wang, Z. Zhang, Review on chloride transport in alkali-activated materials: role of precursors, activators and admixtures, Constr. Build. Mater. 328 (2022) 127081.
[3] W. Cai, Z. Xu, Z. Zhang, J. Hu, H. Huang, Y. Ma, Z. Zhang, H. Wang, S. Yin, J. Wei, Chloride binding behavior of synthesized reaction products in alkali-activated slag, Compos. Part B Eng. 238 (2022) 109919.
[4] W. Tahri, X. Hu, C. Shi, Z. Zhang, Review on corrosion of steel reinforcement in alkali-activated concretes in chloride-containing environments, Constr. Build. Mater. 293 (2021) 123484.
[5] J. Hu, S. Zhang, E. Chen, W. Li, A review on corrosion detection and protection of existing reinforced concrete (RC) structures, Constr. Build. Mater. 325 (2022) 126718.
[6] Y. Zhang, G. Ye, Z. Yang, Pore size dependent connectivity and ionic transport in saturated cementitious materials, Constr. Build. Mater. 238 (2020) 117680.
[7] Q. Yuan, C. Shi, G. De Schutter, K. Audenaert, D. Deng, Chloride binding of cement-based materials subjected to external chloride environment–a review, Constr. Build. Mater. 23 (1) (2009) 1–13.
[8] Z. Yang, H. Fischer, R. Polder, Laboratory investigation of the influence of two types of modified hydrotalcites on chloride ingress into cement mortar, Cem. Concr. Compos. 58 (2015) 105–113.
[9] J.L. Provis, S.A. Bernal, Geopolymers and related alkali-activated materials, Annu. Rev. Mater. Res. 44 (2014) 299–327.
[10] M.R. Rowles, J.V. Hanna, K.J. Pike, M.E. Smith, B.H. O'Connor, 29Si, 27Al, 1H and 23Na MAS NMR study of the bonding character in aluminosilicate inorganic polymers, Appl. Magn. Reson. 32 (4) (2007) 663–689.
[11] X. Ke, S.A. Bernal, J.L. Provis, Uptake of chloride and carbonate by Mg-Al and Ca-Al layered double hydroxides in simulated pore solutions of alkali-activated slag cement, Cem. Concr. Res. 100 (2017) 1–13.
[12] J. Zhang, Y. Ma, J. Zheng, J. Hu, J. Fu, Z. Zhang, H. Wang, Chloride diffusion in alkali-activated fly ash/slag concretes: role of slag content, water/binder ratio, alkali content and sand-aggregate ratio, Constr. Build. Mater. 261 (2020) 119940.
[13] N. Lee, H.-K. Lee, Influence of the slag content on the chloride and sulfuric acid resistances of alkali-activated fly ash/slag paste, Cem. Concr. Compos. 72 (2016) 168–179.
[14] M. Babaee, A. Castel, Chloride diffusivity, chloride threshold, and corrosion initiation in reinforced alkali-activated mortars: role of calcium, alkali, and silicate content, Cem. Concr. Res. 111 (2018) 56–71.
[15] J. Zhang, C. Shi, Z. Zhang, Chloride binding of alkali-activated slag/fly ash cements, Constr. Build. Mater. 226 (2019) 21–31.
[16] I. Ismail, S.A. Bernal, J.L. Provis, R. San Nicolas, D.G. Brice, A.R. Kilcullen, S. Hamdan, J.S. van Deventer, Influence of fly ash on the water and chloride permeability of alkali-activated slag mortars and concretes, Constr. Build. Mater. 48 (2013) 1187–1201.
[17] A.M. Neville, Properties of Concrete, Longman London1995.
[18] Y. Chen, Z. Shui, W. Chen, G. Chen, Chloride binding of synthetic Ca–Al–NO3 LDHs in hardened cement paste, Constr. Build. Mater. 93 (2015) 1051–1058.
[19] X. Bi, H. Zhang, L. Dou, Layered double hydroxide-based nanocarriers for drug delivery, Pharmaceutics 6 (2) (2014) 298–332.
[20] S.-w Choi, B.-s Jang, J.-h Kim, K.-m Lee, Durability characteristics of fly ash concrete containing lightly-burnt MgO, Constr. Build. Mater. 58 (2014) 77–84.
[21] Z.H. Shui, J.T. Ma, W. Chen, X. Gao, The Effect of Layered Double Hydroxides on the Concrete Resistance of Chloride-ion Penetration. Key Engineering Materials, 2012, pp. 99–105.
[22] B. Li, S. Zhang, Q. Li, N. Li, B. Yuan, W. Chen, H. Brouwers, Q. Yu, Uptake of heavy metal ions in layered double hydroxides and applications in cementitious materials: experimental evidence and first-principle study, Constr. Build. Mater. 222 (2019) 96–107.
[23] Y. Chen, R. Yu, X. Wang, J. Chen, Z. Shui, Evaluation and optimization of Ultra-High Performance Concrete (UHPC) subjected to harsh ocean environment: towards an application of Layered Double Hydroxides (LDHs), Constr. Build. Mater. 177 (2018) 51–62.
[24] P. Duan, W. Chen, J. Ma, Z. Shui, Influence of layered double hydroxides on microstructure and carbonation resistance of sulphoaluminate cement concrete, Constr. Build. Mater. 48 (2013) 601–609.
[25] H. Yoon, S.M. Park, H.-K. Lee, Effect of MgO on chloride penetration resistance of alkali-activated binder, Constr. Build. Mater. 178 (2018) 584–592.
[26] T. Liu, Y. Chen, Q. Yu, J. Fan, H. Brouwers, Effect of MgO, Mg-Al-NO3 LDH and calcined LDH-CO3 on chloride resistance of alkali activated fly ash and slag blends, Constr. Build. Mater. 250 (2020) 118865.
[27] X. Ke, S.A. Bernal, O.H. Hussein, J.L. Provis, Chloride binding and mobility in sodium carbonate-activated slag pastes and mortars, Mater. Struct. 50 (6) (2017) 252.
[28] Y. Wang, K. Fu, Comparisons of instantaneous chloride diffusion coefficients determined by RCM method and chloride natural diffusion test, Constr. Build. Mater. 223 (2019) 595–604.
[29] X. Ke, S.A. Bernal, J.L. Provis, Controlling the reaction kinetics of sodium carbonate-activated slag cements using calcined layered double hydroxides, Cem. Concr. Res. 81 (2016) 24–37.
[30] Y. Cao, D. Zheng, S. Dong, F. Zhang, J. Lin, C. Wang, C. Lin, A composite corrosion inhibitor of MgAl layered double hydroxides co-intercalated with hydroxide and organic anions for carbon steel in simulated carbonated concrete pore solutions, J. Electrochem. Soc. 166 (11) (2019). C3106.
[31] L. Guo, Y. Wu, P. Duan, Z. Zhang, Improving sulfate attack resistance of concrete by using calcined Mg-Al-CO3 LDHs: adsorption behavior and mechanism, Constr. Build. Mater. 232 (2020) 117256.
[32] T.T.X. Hang, T.A. Truc, N.T. Duong, N. Pébère, M.-G. Olivier, Layered double hydroxides as containers of inhibitors in organic coatings for corrosion protection of carbon steel, Prog. Org. Coat. 74 (2) (2012) 343–348.
[33] X. Hu, C. Shi, Z. Shi, L. Zhang, Compressive strength, pore structure and chloride transport properties of alkali-activated slag/fly ash mortars, Cem. Concr. Compos. 104 (2019) 103392.
[34] E.P. Barrett, L.G. Joyner, P.P. Halenda, The determination of pore volume and area distributions in porous substances. I. Computations from nitrogen isotherms, J. Am. Chem. Soc. 73 (1) (1951) 373–380.
[35] J. Geng, C. Pan, Y. Wang, W. Chen, Y. Zhu, Chloride binding in cement paste with calcined Mg-Al-CO3 LDH (CLDH) under different conditions, Constr. Build. Mater. 273 (2021) 121678.
[36] C. Hall, Water movement in porous building materials—I. Unsaturated flow theory and its applications, Build. Environ. 12 (2) (1977) 117–125.
[37] Y. Wang, Y. Cao, P. Zhang, Y. Ma, T. Zhao, H. Wang, Z. Zhang, Water absorption and chloride diffusivity of concrete under the coupling effect of uniaxial compressive load and freeze–thaw cycles, Constr. Build. Mater. 209 (2019) 566–576.
[38] F. Jin, K. Gu, A. Al-Tabbaa, Strength and drying shrinkage of reactive MgO modified alkali-activated slag paste, Constr. Build. Mater. 51 (2014) 395–404.
[39] F. Jin, K. Gu, A. Al-Tabbaa, Strength and hydration properties of reactive MgO-activated ground granulated blastfurnace slag paste, Cem. Concr. Compos. 57 (2015) 8–16.
[40] C.-L. Hwang, D.-H. Vo, V.-A. Tran, M.D. Yehualaw, Effect of high MgO content on the performance of alkali-activated fine slag under water and air curing conditions, Constr. Build. Mater. 186 (2018) 503–513.
[41] J.F. Young, S. Mindess, D. Darwin, Concrete, Prentice Hall2002.
[42] S.-W. Pack, M.-S. Jung, H.-W. Song, S.-H. Kim, K.Y. Ann, Prediction of time dependent chloride transport in concrete structures exposed to a marine environment, Cem. Concr. Res. 40 (2) (2010) 302–312.
[43] N. Lee, H.-K. Lee, Setting and mechanical properties of alkali-activated fly ash/slag concrete manufactured at room temperature, Constr. Build. Mater. 47 (2013) 1201–1209.
[44] S. Park, H.M. Park, H. Yoon, J. Seo, C.-M. Yang, J.L. Provis, B. Yang, Hydration kinetics and products of MgO-activated blast furnace slag, Constr. Build. Mater. 249 (2020) 118700.

[45] G. Glass, N. Buenfeld, Chloride-induced corrosion of steel in concrete, Prog. Struct. Eng. Mater. 2 (4) (2000) 448–458.
[46] Y. Wang, Y. Cao, Y. Ma, S. Xiao, J. Hu, H. Wang, Fresh and hardened properties of alkali-activated fly ash/slag binders: effect of fly ash source, surface area, and additives, J. Sustain. Cem. Based Mater. (2021) 1–24.
[47] M. Kruk, M. Jaroniec, Gas adsorption characterization of ordered organic− inorganic nanocomposite materials, Chem. Mater. 13 (10) (2001) 3169–3183.
[48] P. Zhang, F.H. Wittmann, M. Vogel, H.S. Müller, T. Zhao, Influence of freeze-thaw cycles on capillary absorption and chloride penetration into concrete, Cem. Concr. Res. 100 (2017) 60–67.
[49] Z. Shi, C. Shi, S. Wan, N. Li, Z. Zhang, Effect of alkali dosage and silicate modulus on carbonation of alkali-activated slag mortars, Cem. Concr. Res. 113 (2018) 55–64.
[50] A.E. Morandeau, C.E. White, Role of magnesium-stabilized amorphous calcium carbonate in mitigating the extent of carbonation in alkali-activated slag, Chem. Mater. 27 (19) (2015) 6625–6634.
[51] S. Song, H.M. Jennings, Pore solution chemistry of alkali-activated ground granulated blast-furnace slag, Cem. Concr. Res. 29 (2) (1999) 159–170.
[52] C. Tennakoon, A. Shayan, J.G. Sanjayan, A. Xu, Chloride ingress and steel corrosion in geopolymer concrete based on long term tests, Mater. Des. 116 (2017) 287–299.
[53] T. Yang, X. Yao, Z. Zhang, Quantification of chloride diffusion in fly ash–slag-based geopolymers by X-ray fluorescence (XRF), Constr. Build. Mater. 69 (2014) 109–115.
[54] H. Ma, X. Li, X. Zheng, X. Niu, Y. Fang, Effect of active MgO on the hydration kinetics characteristics and microstructures of alkali-activated fly ash-slag materials, Constr. Build. Mater. 361 (2022) 129677.
[55] S. Yoon, J. Moon, S. Bae, X. Duan, E.P. Giannelis, P.M. Monteiro, Chloride adsorption by calcined layered double hydroxides in hardened Portland cement paste, Mater. Chem. Phys. 145 (3) (2014) 376–386.
[56] G. Ye, Percolation of capillary pores in hardening cement pastes, Cem. Concr. Res. 35 (1) (2005) 167–176.